On-ground calibration highlights for the SVOM/ECLAIRs camera

Godet O.[a], Atteia J.-L.[a], Amoros C.[a], Roger P.[a], Bouchet L.[a], Dezalay J.-P.[a], Yassine M.[a], Arcier B.[a], Bordon S.[a], Lacombe K.[a], Lecomte E.[a], Llamas M.[a], Maestre S.[a], Marty W.[a], Papais S.[a], Ramon P.[a], Verdeil C.[a], Waegebaert V.[a], Schanne S.[b], Dagoneau N.[b], Chateau F.[b], Kestener P.[b], Le Provost H.[b], Tahoulan C.[b], Cordier B.[b], Tourrette Th.[b], Daly F.[b], Triou H.[b], Coleiro A.[c], Goldwurm A.[c], Lachaud C.[c], Guillemot Ph.[d], Mouret J.-M.[d], Charmeau M.-C.[d], Perraud L.[d], Bousquet F.[d], Cervantes Y.[d], Gasc Ph.[d], Pasquier H.[d], Perrin L.[d], Ruellan M.[d], Simonella O.[d], and Yadallee M.[d]

[a]IRAP, CNRS/UPS/CNES, 9 avenue du colonel Roche, 31028 Toulouse, France
[b]CEA-Saclay, IRFU, F-91191, Gif-sur-Yvette, France
[c]Université Paris Cité, CNRS, CEA, Astroparticule et Cosmologie, F-75013 Paris, France
[d]CNES, 18 Av. Edouard Belin, 31401 Toulouse cedex 9, France

ABSTRACT

The Chinese-French mission SVOM due to be launched in 2023 is the next generation of missions fully dedicated to the survey of the transient sky thanks to an agile spacecraft embarking a multi-wavelength science payload associated with a network of ground robotic nIR/optical telescopes. The SVOM core instrument is the 4–150 keV 2-D coded mask camera ECLAIRs responsible for the autonomous search and trigger of transient events within its field of view. The flight model of ECLAIRs has been built by several French labs (IRAP, CEA, APC) under the supervision of the French Space Agency (CNES). In 2021, intensive on-ground calibration has been performed on the ECLAIRs camera. Here, we give an overview of the calibration sequences of the ECLAIRs flight model and we present an overview of the main instrument performances.

Keywords: space mission, SVOM, high energy, Gamma-ray burst, instrumentation, calibration, coded mask

1. INTRODUCTION

1.1 The SVOM mission

The Chinese-French Space-based multi-band Variable Object Monitor mission [1] is dedicated to the study of the high-energy transient sky with a particular interest for Gamma-ray bursts [2,3] (GRBs). These extreme phenomena are the most powerful cosmological (up to z $\sim$ 9.4[4]) explosions signaling the catastrophic formation of a stellar-mass black hole (BH) or a neutron star (NS) and the launch of powerful ultra-relativistic jets following the core-collapse of some massive stars with masses larger than 30 $M_\odot$[5] or the merger of two NSs/NS-BH.[6] The later GRB progenitors are also very strong emitters of gravitational waves (GW) as shown by the detection of the exceptional event GW 170817 associated with the off-axis short GRB 170817A.[7] With a launch expected at the end of 2023, SVOM will work in synergy with game-changer multi-messenger facilities (e.g. Ligo/Virgo/Kagra in GWs, IceCube/KM3Net in neutrinos, Vera Rubin Observatory/LSST, SKA, CTA for the transient sky in optical, radio and very high energies respectively, JWST & E-ELT for the high-redshift Universe). SVOM will be operated like the *Neil Gehrels Swift* observatory[8] i.e. an agile spacecraft carrying a multi-wavelength science payload with two wide-field instruments: ECLAIRs,[9] the GRB trigger camera, and the Gamma-Ray Monitor (GRM)[10,11] to study the GRB prompt emission from 4 keV to 5 MeV as well as two narrow-field instruments: the 0.2–10 keV Micro-channel plate X-ray Telescope[12,13] (MXT) and the Visible Telescope[14] (VT) in order to

Further author information: (Send correspondence to O. Godet)
O. Godet: E-mail: ogodet@irap.omp.eu, Telephone: +33 561557536

follow-up the afterglow emission of detected events in both X-rays and R & B bands, respectively – see Figure 1. Once ECLAIRs will trigger on a new transient appearing within its field of view (FoV) in an autonomous way, the spacecraft will swiftly and automatically repoint MXT and VT towards the ECLAIRs source position ($< 13'$ at 90% confidence level) in order to refine its localization with accuracy below a dozen of arc-seconds in X-rays and < 1 arc-second in optical. In addition to the space observing segment, SVOM will also include a series of wide-/narrow-field robotic telescopes (i.e. the Ground Wide Angle Cameras[15] & the Chinese Ground Follow-up Telescope working in optical and Colibri[16] working in both optical and near IR with the CAGIRE camera[17]) spread around the SVOM LEO orbit. In order to maximize the number of GRBs with measured spectroscopic redshift as well as not to reduce too much the ECLAIRs sensitivity to GRBs, SVOM will use a complex attitude law so that the nominal pointing of ECLAIRs is anti-Sun with general avoidance of the Galactic center, Sco X-1 and the Moon within its FoV. This means that the Earth will pass several times per day through the instrument FoV.

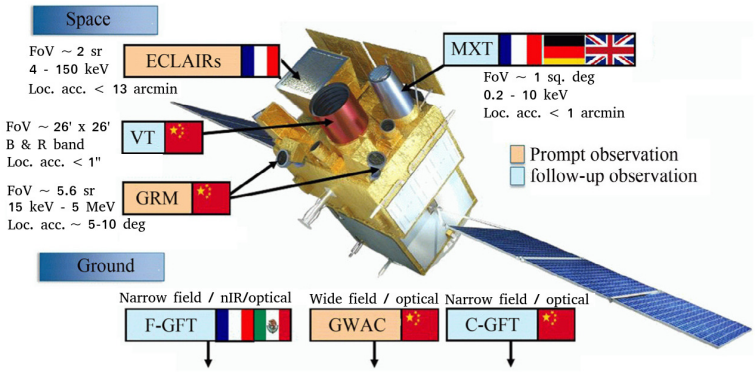

Figure 1. SVOM science payload and ground segment.

1.2 The GRB trigger camera ECLAIRs

The prime instrument onboard SVOM is the wide-field (~ 2 sr) coded-mask imager ECLAIRs[9] responsible for autonomously detecting GRBs and other high-energy transients and providing their first localization to the ground (see Fig. 2). ECLAIRs is part of a collaboration between several French labs (IRAP, CEA-Saclay and APC) with a science lead by IRAP and a supervision from the French Space Agency (CNES).

The detection plane built by IRAP has a moderate geometrical surface of almost 1000 cm^2. To enhance the ECLAIRs sensitivity to soft X-ray bursts and high-redshift GRBs [18], ECLAIRs will start observing photons from 4 keV up to 150 keV. This requested value of the low-energy threshold had some major impacts on the instrument design as described below and drove a large fraction of the performance and calibration tests performed on the flight model (see Sections 2 & 4). The detection plane is divided into 8 sectors for redundancy purpose. Each sector gathers 25 detection modules [19], so-called XRDPIX. On each module, the 4×4 mm^2 and 1 mm-thick Schottky-type CdTe detectors from Acrorad Ltd will be arranged into a 8×4 detector matrix coupled with the CEA low-noise and low consumption ASIC IDeF-X [20–22]. XRDPIX modules are mounted on a large AlBeMet cold plate.

Each sector is connected to an electrically independent readout electronics (ELS) that works in the photon counting mode: each event detected above the low-energy threshold is time-tagged with a resolution of 20 μs, position-tagged on the plane and its energy is encoded over a 10 bit dynamics depending on its type. Events in the channel 1023 are considered as saturating events. The ELS also performs pattern recognition flagging the events as single or multiple events in order to screen "true" photons hitting the detectors (single events) from other events induced by fluorescence & Compton interaction processes and particle showers onto the plane. These single events are used by the data processing unit (UGTS) to build shadowgrams (i.e. projected images of the coded mask onto the plane) in different energy bands and over different timescales and further used by the onboard count rate and image trigger algorithms (provided by the CEA-Saclay) to autonomously search in near

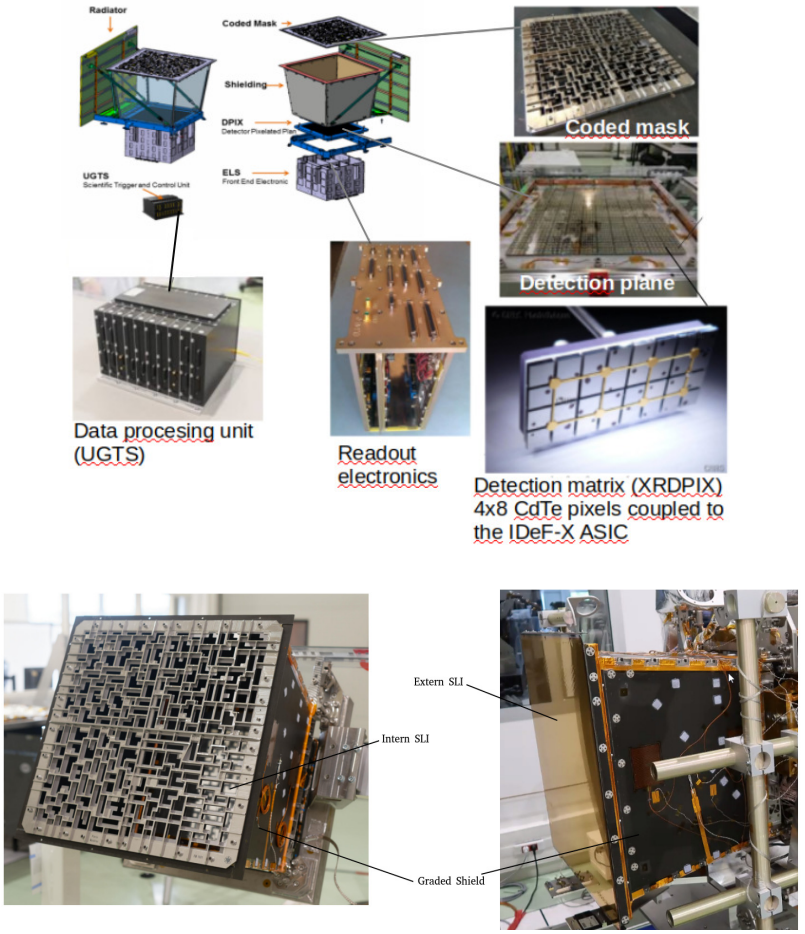

Figure 2. Top – ECLAIRs flight sub-systems: Structure & Pb/Cu shield, Detection plane (6400 Schottky-type CdTe pixels), Coded mask & On-board data processing unit including the GRB trigger algorithms (UGTS). Bottom – Pictures of the ECLAIRs flight model camera.

real-time for the appearance of transient sources [e.g. 23]. The multiple events are detected at the XRDPIX and sector level over a 3.2 μs or 1μs coincidence time window respectively. Once an event is read by the ELS, further incoming photons on the readout XRDPIX module will be lost for some time. In order to reduce the dead time during the readout process, the ELS does not encode the energy of all the detected multiple events. In practice, we chose to only keep energy information for double events called MEC (Multiple Events with encoded Energy) since they carry information about fluorescence interactions within detectors that will be useful for in-flight calibration activities. For other multiple events, the electronics only records their detection time and either the number of pixels hit within a XRDPIX module (MEA) or the number of XRDPIX modules hit over a sector (MEE). The readout electronics is designed to support an event flow from an extremely bright GRB up to 5×10^4 events s^{-1} over the whole detection plane with a dead time of less than 5%. The main ECLAIRs science requirements of the ECLAIRs instrument are summarized in Figure 3.

ECLAIRs has a large FoV of 89×89 deg^2 which corresponds to ~ 2 steradians, while the totally coded FoV is 22.1×22.1 deg^2 (i.e. ~ 0.15 sr). A graded passive shield built by CNES and supported by a NIDA structure is made of Pb (0.8 mm) & Cu (0.1 mm). This shield encloses the detection plane and the coded mask placed at 46 cm above the plane (see Fig. 2). The materials chosen for the shield will allow for a maximum reduction of the cosmic X-ray diffuse background below 70 keV[18] and to keep a few instrumental X-ray lines from 8 keV to 90 keV for calibration purposes. The ECLAIRs mask built by APC has an aperture fraction of 40% and makes use of a quasi-random pattern. Given the expected low energy threshold of 4 keV, no material supporting the

mask could be used. Instead the mask has been pre-constrained and re-unforced with a cross (see Fig. 2) to mitigate thermo-mechanical deformation. The mask is made of Ta (0.6 mm in thickness) sandwiched by two Ti sheets in order to ensure the flatness and hardness of the mask. In order to prevent optical light to reach the CdTe detectors three SLI covers have been designed: A 25 μm-thick Kapton layer with a $\sim$ 1300 Å-thick SiOx deposit on one face and a 1000 Å-thick Al deposit on the other. SiOx is to mitigate for degradation of the SLI by atomic oxygen along the orbit; Two 12.5 μm-thick Mylar layers with a 1000 Å-thick Al deposit on each face. The latter layers are installed inside the camera cavity and the former one on top of the coded mask with the SiOx deposit facing space (see Fig. 2).

Energy range	4 – 150 keV
Detecting area	~950 cm²
Detectors	6400 CdTe detectors
Total effective area in 10-70 keV	≥340 cm²
Photopeak effective area @ 6 keV	≥200 cm²
Field of view	2.05 sr total
Sensitivity to 1 second long GRB	2.5 10^{-8} erg cm^{-2} s^{-1} in [5–50] keV
Source Localization Error	11.5 arcmin for sces with SNR=8
Energy resolution at 60 keV	< 1.6 keV
Time resolution – dead time	20 µs – <5% for 5 10^4 c/s
single/multiple interaction tagging	
Data acquisition mode	Photon mode
Data rate	≤18Gb/day
Energy calibration accuracy	≤0.3 keV below 80 keV
Additional requirements: Automatically shut noisy pixels ; energy calibration with fluorescence lines from the shield ; on-board imaging & trigger (2 types) ; on-board X-ray source catalog, etc...	

Figure 3. Summary of the main ECLAIRs science requirements.

The detectors are passively cooled through a thermal control system made of CCHP (Constant Conductance Heat-Pipes) installed on the radiator and the cold plate on which the detectors are mounted and VCHP (Variable CHP) making thermal connection between the cold plate and the radiator. The nominal performance temperature range of the detectors is between –25°C and –18°C.

In nominal conditions, ECLAIRs will be always collecting photons except during deep South Atlantic Anomaly (SAA) passages preventing for any meaningful science data to be collected and where the detectors will be depolarized.

2. THE ON-GROUND CALIBRATION SEQUENCES

The long on-ground test sequences to measure the performances of the ECLAIRs detection plane and then of the whole instrument have been built over several years through incremental steps making use of various prototypes of the detection plane. This strategy has enabled us to: 1) Train the AIT and science teams as well as prepare all the ground support equipment (GSE) needed to ensure the tests to run smoothly on the flight model; 2) help refining the exposure times for each test in order to optimize the different test sequences; 3) Build the analysis tools that we used to create the different versions of the calibration & configuration files. The latter files have been used to optimize the setting of the instrument configuration along the test sequences, whereas the calibration files describing the instrument performances will be used for reduction and analysis of in-flight data; 4) Create Monte-Carlo GEANT4-based simulators including complex mass models of our different experimental setups (see Section 3) in order to investigate in more details some issues found in the collected data during the test sequences as well as to build numerical models of the instrument response (e.g. spectral [24] and angular response, dead time [25], etc.) that will be calibrated using the collected experimental data.

Table 1 summarizes the different calibration activities that have been covered through the on-ground test sequences and identifies the flight model sub-systems on which the tests have been performed. The measures performed during the thermal-vacuum (TVAC) tests on the whole instrument allowed us to investigate further

Table 1. Summary of the different performance items measured during the on-ground test sequences for each instrument configurations. Expected in-flight calibration measures to be performed during the commissioning phase are also noted. 'Camera without mask' means that only the shield and the SLI covers were integrated onto the detection plane. 'Full camera' means that the mask has been integrated as well. 'ECLAIRs' means that the full camera including the radiator & the UGTS.

	Detection plane	Camera without mask	Full camera	ECLAIRs	ECLAIRs (in flight)
Low-energy threshold	X				X
Detector efficiency vs energy	X	X			X
Spectral response vs energy	X	X			X (continuum sources)
Angular response	X				X
Shield efficiency vs energy and photon pitch angles			X		X
Mask stopping power vs energy			X	X	X
Transparency of the FoV vs energy		X (with SLI)	X	X	X
Dead time vs photon count rate	X	X			X
Level of optical loading	X		X		X
Imaging efficiency and sensitivity vs energy & source position					X
Statistics of dead and noisy pixels	X	X	X	X	X
Cross-talk	X		X	X	X
Trigger end-to-end test			X		X
Performance stability	X		X	X	X

the long-term stability of the instrument overall performances as well as the performances of the thermal control system. Note that the full imaging performance capabilities of ECLAIRs will be measured in flight during the commissioning phase by pointing various astrophysical targets at different locations within the FoV.

The on-ground test sequences have been carried out through all the year 2021 starting with the measures on the detection plane from 25th of January to 5th of March, followed by measures on the camera (without the coded mask and with the mask) from 30th of April to 26th of May and finally the thermal-vacuum tests on the whole instrument from 5th of October to 29th of October.

3. EXPERIMENTAL SET-UP AND GROUND SEGMENT EQUIPMENT

To perform the test sequences discussed in Section 2, we have put in place several test benches operated in clean rooms in Toulouse (France) – see Figure 4. Most of our performance and calibration measures were carried out using a 2 m-diameter and 3 m-long TVAC chamber installed in one of the CNES clean rooms (see Figs. 4 B). As mentioned in Table 1, we used this chamber to make measures on the detection plane alone, the camera without mask (i.e. shield and SLI covers integrated onto the detection plane) and the full camera (i.e. mask integrated) with all the required GSE (see Figs. 4C & D). In all cases, the UGTS was placed outside the chamber and the radiator was not integrated to the camera. The thermal regulation of the detectors was then achieved through the CCHP being connected to a cold block itself connected to a cryocooler driving the temperature profile and

placed outside the chamber. For TVAC tests, we made use of the larger SIMDIA chamber at Airbus Defense & Space (ADS) to contain the whole ECLAIRs instrument (i.e. including the radiator and the UGTS) and GSE (see Figs. 4 E & F). In this case to regulate the detector temperature (T_{det}), the radiator was facing a radiative surface within the chamber that allowed to simulate different thermal configurations. The thermal control system algorithm in the UGTS was then in charge to maintain the detector temperature from a programmed target temperature (T_{target}). There is roughly a 5°C offset from T_{target} to T_{det}.

These chambers allowed us to operate the detectors and camera in flight conditions (i.e. under vacuum and detectors cooled down to the nominal flight temperature of $T_{det} = -20$°C for most tests). In all cases, the detection plane was installed in a vertical configuration as shown in Figs. 4C & D.

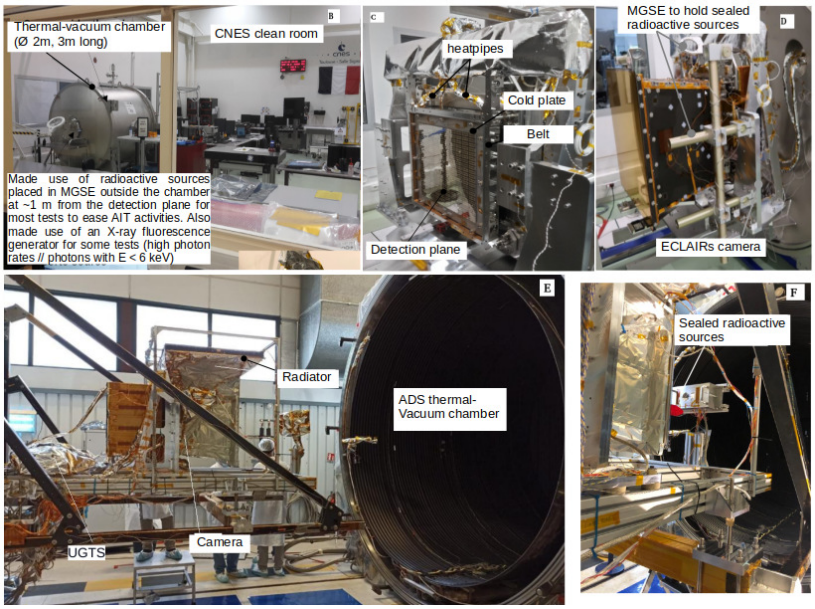

Figure 4. Pictures of the test benches used for the instrument calibration installed in CNES (B) and ADS (F) clean rooms in Toulouse (France). Top: test bench used to make the performance and calibration measures on the detection plane alone (C) and the whole camera (D). Bottom: (E) Bench used to perform TVAC tests on the complete ECLAIRs instrument (including the radiator + UGTS within the chamber). (F) ^{55}Fe+ ^{241}Am sources sealed in a container equipped with a remotely controlled shutter placed within the chamber to perform stability performance measures over time and with changing detector temperatures.

X-ray sources – To illuminate the detectors with X-rays we made use of two types of X-ray sources:

1. Calibrated radioactive sources: ^{55}Fe (5.9 keV), ^{65}Zn (8 keV), ^{241}Am (14–60 keV), ^{133}Ba (4.7, 31, 35, 81 and 356 keV to create saturating events) and ^{57}Co (6.4, 14.4 & 122 keV). This enables to cover almost the entire energy range of ECLAIRs. The source activities have been chosen so that count rates were less than 2 counts s^{-1} pixel^{-1} for most tests to ensure that dead time will not be an issue and that the test exposure times will be at most 1 day to gather enough statistics for data analysis. For radionucleides with short half life, we also made sure that their activity at the end of the test sequences was high enough to avoid too long test exposure times. The selected sources have activity uncertainties from 0.11% (^{241}Am) to 3.7% (^{55}Fe) at 95% confidence level.

   The radioactive sources were in general placed (within a sealed container with a Be front window for radio-protection purposes) outside the thermal-vacuum chamber for tests performed in the CNES clean room to ease AIT activities. For some specific tests where the sources have to be placed inside the chamber (e.g. dead time, TVAC measures), the sources were also placed within a hermetically sealed container with a Be front window. For the TVAC tests, it was also necessary to add heaters on the source container to maintain the sources within their appropriate temperature range as well as a remotely controlled shutter

to create bursts of photons or to perform background spectra. In most cases, the sources were placed along the optical axis of the detection plane and the camera at a distance of about 1 m from the plane when making measures on the detection plane alone and about 1.14 m for the two other model configurations. During the TVAC tests, the sources were at a distance of about 1 m from the plane and slightly off-axis.

2. An X-ray fluorescence generator built by CEA-Saclay and producing a beam of X-ray fluorescent photons in the 4 – 22 keV energy range depending on the target material used (^{21}Sc: 4 keV, ^{22}Ti: 4.5 keV, ^{23}V: 4.9 keV, ^{24}Cr: 5.4 keV, ^{25}Mn: 5.9 keV, ^{26}Fe: 6.4 keV, ^{29}Cu: 8 keV, ^{47}Ag: 22.1 keV). In addition of producing photons with energies below 5.9 keV, important to measure the low-energy effective area (see Figure 5), it was possible to modulate the photon rate produced so that to reach very high count rates on the detection plane ($> 10^5$ counts s^{-1}). This was used to validate some functionalities of the onboard software by simulating bursts & SAA entries [26]. The X-ray generator was fixed at the thermal-vacuum chamber in such a way the photon beam was oriented close to the instrument optical axis. Since it was not possible to precisely know at the time of the measures the exact incoming photon rates, the measures performed on the SLI transparency with the X-ray generator are relative ones to be compared at 5.9 keV and 8 keV with the ones performed with the calibrated radioactive sources.

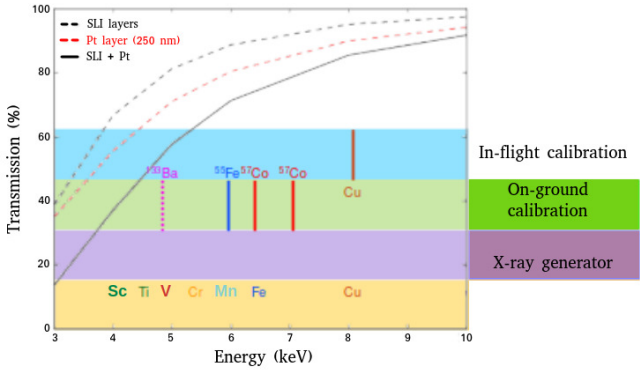

Figure 5. Nominal ECLAIRs low-energy photon transmission profile versus energy. The SLI covers and the Pt cathode absorb photons with energies less than 10 keV. On-ground we used both radioactive sources and an X-ray fluorescence generator to measure the SLI and Pt transmission profile in order to derive the total effective area curve vs energy.

Setting of the detectors – Intensive investigation of the performances of individual XRDPIX modules[27–29] as a function of various setting parameters, the most important ones being the detector high voltage (HV) and the ASIC peaking time ($t_{\rm peak}$) enabled us to define a working point for the XRDPIX modules optimizing their performances: HV $= -300$ V & $t_{\rm peak} = 2.6$ μs. We used this working point for all the performance and calibration measures.

4. CALIBRATION PERFORMANCE HIGHLIGHTS

In this section, we present an overview of the main performance measures done on the detection plane, the telescope and the whole instrument. Forthcoming calibration-dedicated papers will discuss in more details some aspects of the experimental data collected.

The highlights shown in the following sections have been obtained with the detectors being cooled down to $T_{\rm det} = -20°$C except when it is mentioned otherwise. To build data products, we mostly made use of the single event data (see Section 1.2).

4.1 Camera settings

Before starting the performance and calibration measures, we had to set the 6400 low-energy thresholds of the detection plane. To do so, for each pixel we calibrated two linear relations: Channel–Energy (keV) & SBN–$E_{\rm th}$

with SBN, being a number from 0 to 62 setting the low-energy threshold for the electronics and $E_{\rm th}$, being the low-energy threshold in keV.

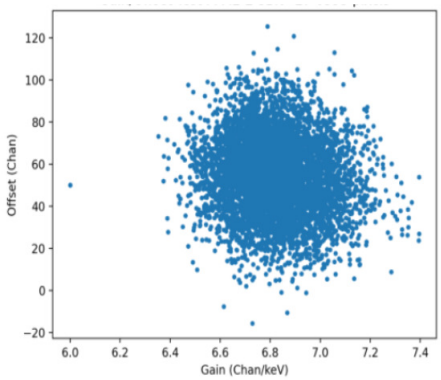

Figure 6. Distribution of the gain & offset coefficients for all the pixels of the detection plane. These coefficients allow to calibrate the recorded event energy in channel into physical unit (keV).

Calibration of the Channel–Energy relation – We built single event ^{55}Fe + ^{241}Am spectrum for each active pixel. We put in place a careful fitting procedure of the lines present in the spectra using either Gaussian lines or more complex line profiles at high energies (e.g. the ^{241}Am 59.5 keV line being distorted on its low-energy side because of charge losses) in order to derive their centroid-values and associated 1 σ errors. At each line centroid-value is associated a line energy in keV. By performing a linear fit to these datapoints, we derived the gain/offset coefficients for each pixel. Figure 6 shows the distribution of the gain–offset coefficients. Note the very homogeneous distribution of the derived coefficients.

Using these coefficients, we were able to compute the energy bound table that will be used by the onboard trigger software to build in near real time shadowgrams in different energy bands from recorded single events. We set five bound energies in keV and we computed the closest corresponding channel-values for each pixel. The table has been uploaded in the UGTS and validated during the on-ground tests (see [26] for more details).

Calibration of the SBN–$E_{\rm th}$ relation – We made ^{55}Fe + ^{241}Am measures with four SBN-values (27, 40, 50, 60) set for all detectors. We built the single event energy-calibrated spectra normalized by the exposure time for each pixel at a given SBN-value using the gain–offset coefficients (see the left panel in Figure 6). We then derived the $E_{\rm th}$-values using a threshold method (here the threshold value was fixed at 3×10^{-3} counts s^{-1}). We computed the A & B coefficients (expressed in keV) of this relation through linear fitting of the SBN–$E_{\rm th}$ points (see the middle panel in Figure 6). The right panel in Figure 6 shows the distribution of the A & B coefficients for one sector (here ELS1) made of 800 detectors. Note again the very good homogeneity of the coefficients. We obtained similar results on the other sectors.

Using the A & B coefficients, we are able to compute the closest SBN-value associated to a given $E_{\rm th}$-value. So, we built the SBN table to be used onboard the UGTS to program the readout electronics such as to have a low-energy threshold of the detectors set at 3.8 keV except for the pixels 8 & 16 of each XRDPIX module (i.e. 400 pixels over the detection plane) for which the low-energy threshold was set at 7 keV. The reason for this is because during performance tests on individual XRDPIX modules we noticed cross-talk between these two adjacent pixels creating multiple events with other pixels of the same module leading to significant loss of single events (see an example of this effect in the left panel of Figure 13). This cross-talk is likely related to the XRDPIX module design and no viable hardware correction could be implemented on the flight model. So, we found that increasing the low-energy threshold of these pixels was a good comprise to mitigate for cross-talk effects. Figure 8 (left) displays the map of the nominal SBN-values that will be used at the launch. Note the white pixels with SBN-values set at 63 corresponding to dead pixels (see Section 4.5) and orange pixels corresponding to XRDPIX pixels 8 & 16 with low-energy threshold set at 7 keV. The SBN-values are very homogeneous for a given $E_{\rm th}$-value as shown in the right panel of Figure 8. Note that we plan to implement onboard the UGTS

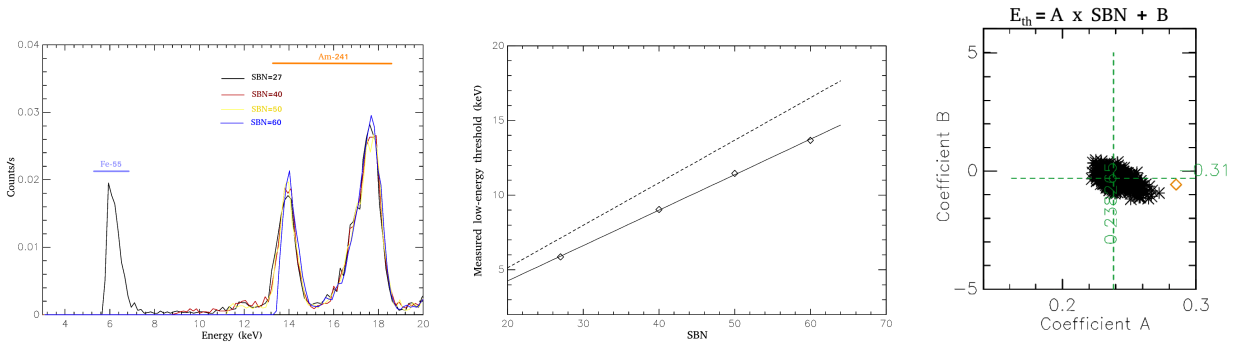

Figure 7. Calibration of the SBN–$E_{\rm th}$ relation. Left – Single event energy-calibrated ^{55}Fe + ^{241}Am spectra at 4 SBN-values for one detector. Note how the low-energy threshold increases with increasing SBN-values. Middle – Linear fit of the SBN–$E_{\rm th}$ points for one pixel. $E_{\rm th}$ is the measured low-energy threshold value in keV at a given SBN value. The dashed line is the expected curve from the ASIC theoretical values of the A & B coefficients. Right – Distribution of the A & B coefficients for one sector (ELS1). The diamond point corresponds to the ASIC theoretical values. The numbers in green are the median values of the A & B coefficients. Note the very homogeneous values between detectors (here 800).

an efficiency map that will allow to correct for any counting discrepancies between pixels in the different energy bands used by the onboard trigger algorithms (see [26] for more details).

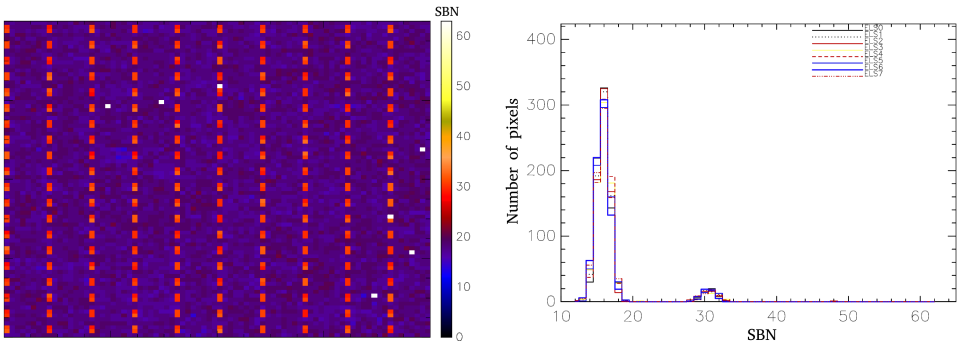

Figure 8. Left – Nominal SBN map to set the low-energy threshold at 3.8 keV for 5994 detectors and at 7 keV for 199 detectors (XRDPIX pixels 8 & 16) for mitigation of cross-talk induced by these two pixels. 7 dead pixels are also present in white (SBN = 63). Right – Distribution of the SBN-values per sector showing a very good homogeneity from pixels to pixels.

Once the SBN table has been uploaded in the UGTS, we re-made a ^{55}Fe + ^{241}Am acquisition to check the accuracy of the low-energy threshold setting. From the single event energy-calibrated spectra, we derived the $E_{\rm th}$-values of all the active pixels in a similar way as explained above. Figure 9 shows the distribution of the reconstructed $E_{\rm th}$-values per sector. The median value of the main peak is at $\sim$ 3.8 keV (with a dispersion of 0.13 keV) as expected. For the second peak we found a median value of $\sim$ 7 keV with a similar dispersion. This demonstrates our capability to set up accurately the low-energy threshold of the ECLAIRs detectors (see Figure 12) in compliance with our science requirements.

4.2 Background spectra

One of our first measures on each model to be tested is to acquire a spectrum from the particle and photon background in order to assess its time stability and its contribution with respect to measures done with X-ray sources. Figure 10 shows the single event energy-calibrated background spectra at three different steps of the test sequences in the CNES clean room: the detection plane alone, the camera without the mask integrated and the full camera. The integration of the shield around the detection plane clearly filtered out part of the incoming

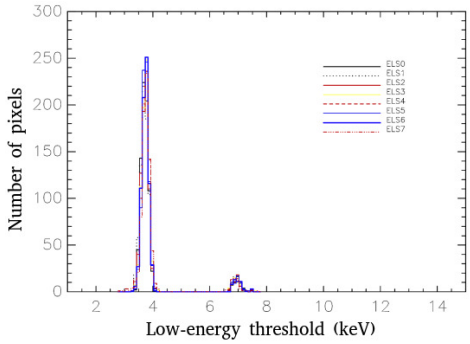

Figure 9. Distribution of the reconstructed $E_{\rm th}$-values per sector.

photon/particle background. In addition to the continuum, several lines are visible corresponding to fluorescence lines from materials around the detectors. After the launch, these lines will be used to monitor on ground the evolution of the energy scale of each active pixel. If a change is found, we will be able to update the onboard configuration and the calibration files used for data reduction and analysis.

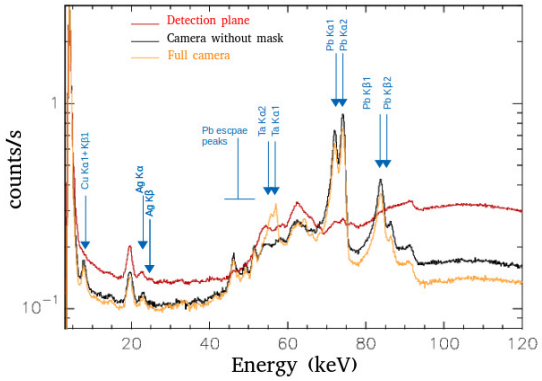

Figure 10. Single event energy-calibrated background spectra on the detection plane alone, the camera without mask and the full camera. The most prominent fluorescence lines from materials around the detectors are also identified.

The background noise count rate appeared to be rather stable over time above 6 keV and negligible with respect to those induced by the various radioactive sources we used (see Fig. 12). Below 6 keV typically, a peak extending down to the low-energy threshold (and sometimes below) could be seen on the three spectra. This is due to a noise contribution that we named Structured Low Energy (SLE) noise excess. We characterized the spatial, temporal and spectral properties of this noise excess. First, this noise excess is not stable from one acquisitions to the other. From the TVAC measures, we computed that its count rate below 6 keV over the entire plane varied from ~ 4 counts s^{-1} to ~ 50 counts s^{-1} (i.e. at maximum, $\sim 19\%$ of the in-flight background noise induced by the cosmic X-ray diffuse background between 4 and 5 keV). This noise affects mostly modules located on the vertical edges of the plane, in particular the pixels in the corners of the modules (see the left panel in Figure 11). We also computed the arrival time differences (ATD) between successive single events for each sector. In a normal case, the ATD distribution should follow an exponential law. The right panel in Figure 11 clearly shows that there is an strong ATD excess below 400 μs induced by this noise excess.

Given its rather low overall count rate, this noise excess did not degrade the classification of incoming photons into single events. Moreover, contributing mostly below 6 keV it did not affect too much the use of the collected performances data.

Our investigation on the origin of this SLE noise excess concluded that it is likely to be induced by a noise source external to the detection plane and its readout electronics. More precisely, we think that even if the exact

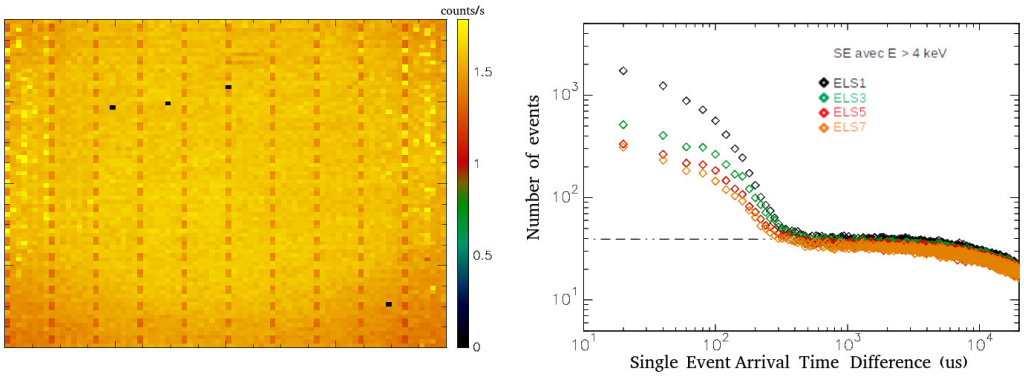

Figure 11. Properties of the SLE noise excess. Left – Single event counting map for an acquisition done on the detection plane alone illuminated by ^{55}Fe + ^{241}Am sources. The SLE noise excess is more intense on the vertical edges of the plane. The pixels appearing in black are dead pixels – See Section 4.5. Given that pixels 8 & 16 have low-energy threshold-values set to 7 keV (see Section 4.1), this accounts for the differences in counting observed on the map for these pixels. Right – Distribution of the single event arrival time differences (ATD) for different sectors (from top right of the plane (ELS1) to bottom right (ELS7)). Note the ATD excesses below 400 μs on all shown sectors. The black dashed-dotted line corresponds to the expected ATD level in log–log space without this noise excess.

coupling is still unknown, it is related to the way the heatpipes work when the detection plane is in the vertical configuration. The heatpipes are actually supposed to nominally work in micro-gravity; which is far from being the case in the vertical configuration. A better configuration would have been to operate the plane in an almost horizontal configuration (see Section 4.3). However, we first did not expect such effect in operating the plane in the vertical configuration at the time. Second, this would have complexified way more our experimental setup and have slowed down the AIT activities. Even if we demonstrated that this SLE noise excess may no longer be an issue in space (see Section 4.3), we investigated some ways to mitigate its effects on the operation of the onboard trigger (by adjusting the trigger setting and adding some data cleaning processes) as well as on the ECLAIRs data reduction pipeline.

4.3 Spectral response

The measures of the spectral response in X-rays and the plane effective area at different energies from 6 keV to 122 keV were one of the central points of the tests performed on the detection plane alone. They were performed by placing the radioactive sources (see Section 3) at a distance of 1 m near the optical axis of the plane. Because the sources being at a finite distance from the plane, this results in a spatial curvature of the event counting over the detection plane (see an example on the left panel in Fig. 11).

Figure 12 shows the superimposition of single event energy-calibrated spectra built per sector (i.e. stacking spectra from 800 pixels) collected on the ECLAIRs detection plane using radioactive sources: ^{55}Fe + ^{241}Am (left) & ^{57}Co (right). Note the overall homogeneity of the spectral response of the CdTe detectors over the entire ECLAIRs energy range! With increasing photon energies the effects of charge losses are clearly visible on the ^{241}Am 59.5 keV and ^{57}Co 122 keV lines.

We also performed some spectral measures at different rotation angles of the detection plane ($\pm 27°$ and $\pm 45°$). The former values rouhgly correspond to the limiting angles for the totally coded part of the FoV, while the latter ones correspond to the limiting angles of the FoV. These measures were only carried out along one rotation axis (i.e. the vertical axis perpendicular to the optical axis of the plane) because of space limitations and GSE constraints within the thermal-vacuum chamber.

There is an intensive on-going work to compare these spectral measures with our Monte-Carlo simulations in order to calibrate our numerical models of the ECLAIRs spectral and angular responses.

As mentioned in Section 4.1, we are able to accurately set the low-energy threshold for each active pixel. However, the presence of the SLE noise excess (see Section 4.2) in most of our on-ground calibration data makes

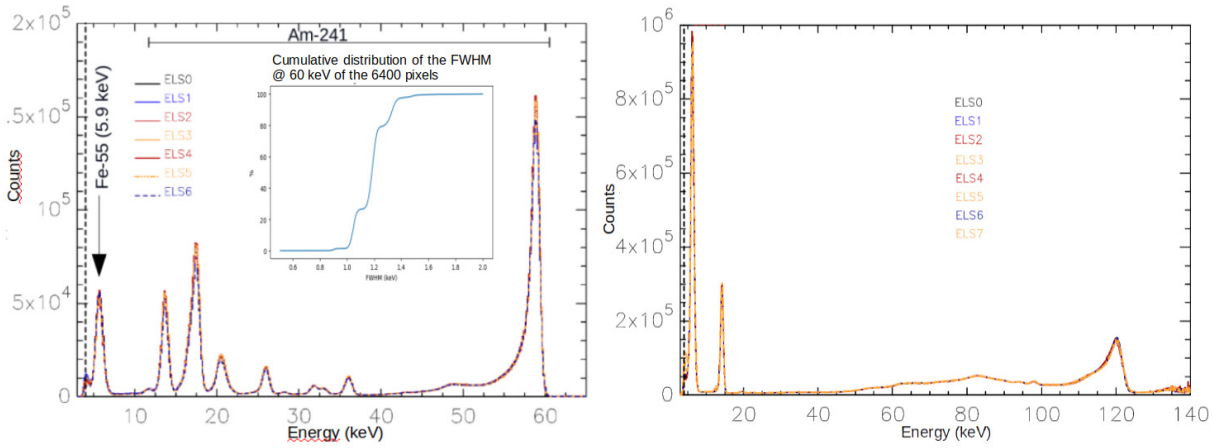

Figure 12. Spectral response over the ECLAIRs energy range. Left – Single event energy-calibrated ^{55}Fe + ^{241}Am spectra built per sector (i.e. by stacking 800 individual spectra). The close-up displays the cumulative distribution of the ^{241}Am 59.5 keV FWHM. Right – The same thing using a ^{57}Co source. The vertical dashed line in both plots indicates 4 keV.

it difficult to assess that the main contribution of the electronic noise is restricted to E $<$ 4 keV.

Measures on individual XRDPIX modules have shown a very strong relationship[27] between the measured low-energy threshold in keV (based on the contribution of the electronic noise) and the ^{241}Am 59.5 keV FWHM. As long as the FWHM(59.5 keV)-values are below 1.6 keV, the contribution of the electronic noise shall be less than 4 keV. Spectral fitting of the ^{241}Am 59.5 keV line enabled us to derive the FWHM-values of each active pixels on the flight model. The cumulative distribution of the FWHM(59.5 keV) is shown in the left panel of Figure 12. $\sim$ 99.5% of the ECLAIRs detectors have a FWHM less than 1.6 keV! This result ensures that the electronic noise contribution is less than 4 keV for most detectors in compliance with our science requirements.

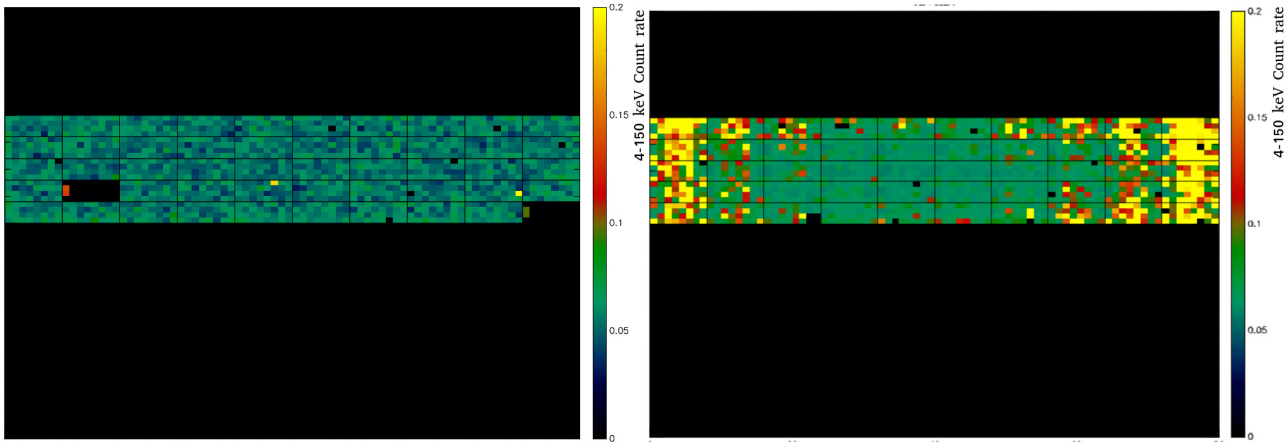

Figure 13. Single event counting maps in the 4–150 keV band built from data collected on the spare model of the detection plane (see text). Left – With the plane being almost horizontal. Right – With the plane being vertical. No radioactive source was used for the two acquisitions. No SLE noise excess visible when the plane is in the horizontal configuration. The pixels appearing in black are disabled pixels. On the left map, modules appearing in dark are because pixels 8 & 16 of these modules created multiple events with the other pixels of the modules.

In order to further understand the origin of the SLE noise excess, we performed some measures on the spare model of the detection plane that will be used to investigate issues with the flight model once in space as well as to validate some commands and patches of the on-board software. This model is made of only two complete

sectors each one coupled with an ELS readout electronics. This model is operated the same way as the flight model and we re-used the same experimental GSEs as the ones used in the CNES clean room for the calibration of the flight model. The XRDPIX modules that equipped this model were manufactured the same way as the ones paving the flight model, but presented less good performances. After several investigation it appears that operating the heatpipes cooling down the detectors in a vertical configuration is not optimal since they are supposed to work under micro-gravity. However, at the time it was not possible to place the flight model in a almost horizontal configuration to mimic a micro-gravity environment. So we did it on the ground model. The background measures we performed clearly show that in this configuration the SLE noise excess completely disappeared. This noise reappears once we have putting back the plane in the vertical configuration as shown in the right panel of Figure 13. Figure 14 shows the single event energy-calibrated spectra over the plane (for active pixels) in the 0–20 keV band for the horizontal (orange) and vertical (black) configurations of the plane. The SBN-values of each active pixel have been set such that their low-energy threshold values are around 4 keV. Note that the SLE noise excess is no longer visible in the horizontal configuration.

This clearly demonstrates that overall the electronic noise of the detectors on the flight model is less than 4 keV in agreement with the FWHM(59.5 keV) cumulative distribution. Moreover, we may hope that the heatpipes working nominally in micro-gravity in space the SLE noise excess will not be present. In any case, we will be vigilant to assess the presence of this noise component from the first collected data.

Figure 14. Single event energy-calibrated spectra of all the active pixels of the plane in the horizontal (orange) & vertical (black) configurations of the detection plane. No radioactive source was used for the two acquisitions done on the ground model of the detection plane. In the horizontal configuration, the SLE noise excess is no longer visible.

4.4 Effective area

From the measures at different energies across the ECLAIRs energy range, we were also able to derive the way the photo-peak effective area of the detection plane varies with photon energy and to compare it to Monte-Carlo GEANT4-based simulations (see Figure 15). The simulations were performed using a detailed mass model of the detection plane illuminated by an on-axis point-like source at infinity. To derive the effective area from the experimental data, we applied various corrections to them [30], in particular the solid angle correction since the radioactive sources were not located at infinity. As shown in Figure 15, the experimental datapoints agree very well with the simulations at a level better than 5%; which is very good and compliant with our calibration requirements to reach a 10% level accuracy.

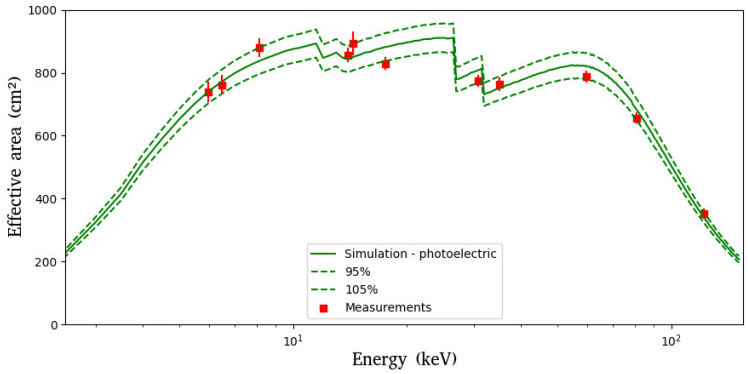

Figure 15. Photo-peak effective area of the ECLAIRs detection plane vs photon energy: (red points) as measured on the flight model illuminated by various on-axis radioactive sources (^{55}Fe, ^{65}Zn, ^{133}Ba, ^{241}Am and ^{57}Co) and (solid curve) as simulated using GEANT4 and the detailed mass model of the detection plane. The dashed lines give the envelop at ±5% from the solid line. Note the overall very good agreement between the experimental datapoints and the simulations.

We also made some measures at low-energies (below 10 keV) with on-axis radioactive sources (^{55}Fe, ^{65}Zn) illuminating the detection plane with the SLI covers placed in front of it (the model configuration "camera without mask") in order to measure the SLI transparency as function of photon energy. This is an important point to ensure that the total effective area of the camera below 10 keV is compliant with our science requirements (see Section 1.2). We also performed measures with the X-ray fluorescence generator between 4 and 10 keV to complete the SLI transparency curve. The data analysis and comparison to our simulations are on-going. The results will be further discussed in [30].

4.5 Noisy & dead pixels

There are several reasons for a pixel to become noisy [27]: 1) its low-energy threshold is not adequately set; 2) Cross-talk could give rise to particular pixel behavior like for the pixels 8 & 16 of the XRDPIX modules; 3) The pixel displays some unstable behavior (i.e. its count rate can suddenly increase for a while before calming itself down, but not always – see the left panel in Figure 16). In this latter case even if the physical origin of this instability is still unknown, we observed that the number of these noisy pixels strongly depends on the values of the ASIC peaking time and the detector high voltage [27, 29]. The varieties 2) and 3) of noisy pixels have been observed during the performance tests. Adapting the value of the pixel low-energy threshold for case 2) noisy pixels was in most cases enough to calm them.

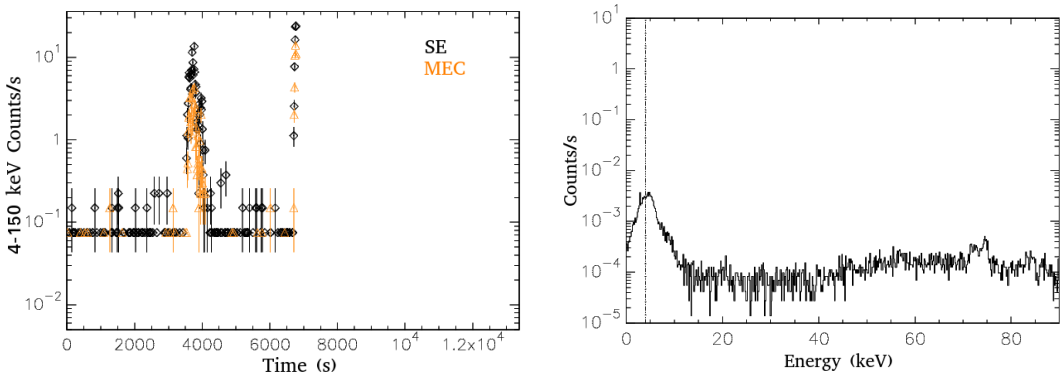

Figure 16. Left – 4–150 keV lightcurve of a very noisy pixel (in black single events and in orange MEC events). Note that the noisy pixel is disabled during the acquisition when its total count rate is larger than 25 cts s^{-1}. Right – Single event background spectrum of the same noisy pixel. Note that in this particular case, the noise peak extends below the low-energy threshold marked by the dotted-dashed vertical line.

We have implemented in the UGTS an algorithm allowing to disable noisy pixels on the detection plane in a dynamical way. We did so because very noisy pixels could deeply affect the behavior of the onboard trigger algorithms. In practice, this algorithm only disables one very noisy pixel over the whole plane every 8 s when its total count rate is larger than 25 counts s^{-1} (i.e. 200 counts over 8 s) – see Figure 16. This prevents for instance to disable several detectors by mistake following a particle shower event hitting the detection plane for instance. In addition, this software could not disable more than a certain number of pixels on the plane (set at 640 detectors i.e. 10% of the plane detectors). Once disabled the very noisy pixels will no longer be considered by the readout electronics. In flight, we plan to give a chance to dynamically disabled very noisy pixels by resetting their low-energy threshold to their initial value once SVOM will exit a deep SAA passage. If these pixels become noisy again they will be again disabled and so on.

From the ground each week, we will be able at the Eclairs Instrument Centre (EIC) to prepare a new dead pixel table taking into account the behavior of the measured disabled pixels. Note that a dead pixel will be always discarded by the onboard readout electronics. Its status can only be changed by uploading a new dead pixel table from the ground. Before setting a noisy pixel as a dead pixel, it is possible to adjust its low-energy threshold to reduce the likelihood for this pixel to become noisy again.

Over the whole test sequences, only 7 pixels over 6400 were set as dead pixels because they were systematically disabled by the software. Overall, very noisy pixels are relatively rare events. During the TVAC tests

accumulating 7 days of performance data, we measured less than 80 disabled noisy pixels. From these, only a few (< 10) were disabled more than once. We will keep an eye on those pixels once in space.

4.6 Impacts of optical light loading

Given that the CdTe detectors are very sensitive to optical light, we performed some measures with X-ray and optical photons illuminating the detection plane to investigate how optical light would affect the X-ray spectral response and if any remanence effects on the X-ray spectral response could be measured once the optical light is switched off. These measures also allowed us to investigate the limits of the readout electronics in processing high incoming photon rates.

Once the optical light is switched on for around 20 min, the count rates of single and multiple (MEC) events instantaneously reached up to $> 2 \times 10^5$ counts s^{-1} (see Figure 17 top left). The level of multiple events reached $\sim 25\%$. The readout electronics nicely processed this large data flow. About 200 pixels were disabled during this time period because being considered too noisy. Spectrally, we note the presence of a very prominent peak extending well below the low-energy threshold. Once the optical light is switched off, no remanence effect on the X-ray spectral response was observed. The count rate over the plane promptly resumed to its initial value. Spectrally the X-ray spectra look like the ones prior to the illumination by optical photons (see Figure 17 top right).

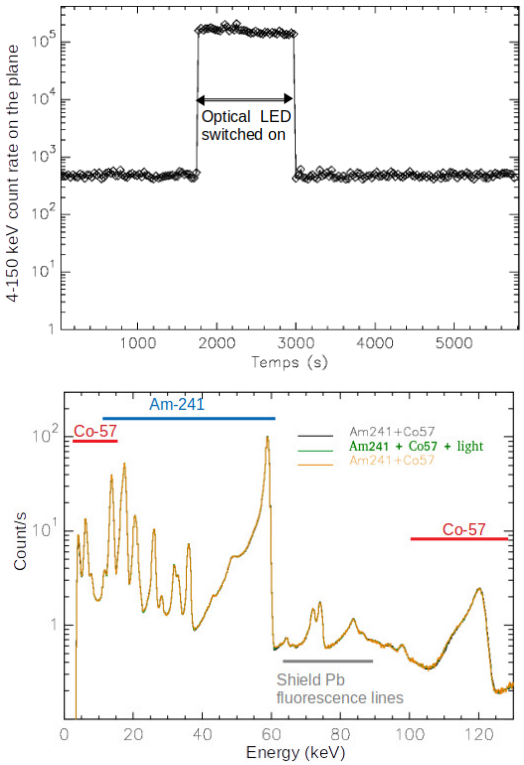

Figure 17. (a) 4–150 keV lightcurve of single and MEC events. Data collected without X-ray sources and with/without optical light. (b) Corresponding spectra acquired before, during and after the LED has been switched on. Note the distortion of the X-ray spectral response due to optical light. Once the LED has been switched off, no remanence effect is observed on the X-ray spectral response (blue curve). The dashed vertical line is placed at 4 keV. (c) ^{241}Am + ^{57}Co X-ray spectra acquired with the full camera being illuminated with and without optical photons from a ~ 10 kLux lamp. No distortion on the X-ray spectral response is seen meaning that the camera cavity is indeed fully dark.

Given the anti-Sun pointing of SVOM, the Earth will regularly pass through the ECLAIRs FoV. The shield and the two SLI covers (see Section 1.2) are supposed to prevent optical loading on the detectors. To verify this

at the camera level, we performed some measures using X-rays (^{241}Am + ^{57}Co) with and without a $\sim$ 10 kLux 4000 K lamp emitting optical photons to roughly mimic the Earth Albedo. No distortion of the X-ray spectral response has been seen indicating that the ECLAIRs cavity is indeed fully dark (see Figure 17 bottom).

4.7 Performance stability

The polarization effect – Schottky-type CdTe detectors are known to suffer from the polarization effect[31] when reversely biased leading to a degradation of their spectral performances over time (see the left and middle panels in Figure 18). This is due to the accumulation of holes closed to the cathode over time. When the electric field in the depth of the detector cancels at the cathode, the detectors are no longer fully depleted and charges created by photon energy deposits close to the cathode start to be partially or totally lost degrading the entire spectral response and counting efficiency of the detectors. The polarization effects will propagate from low to high energies. The time when the degradation starts to become important (i.e. the polarization time t_p) strongly depends on the detector temperature and the value of the bias voltage applied to the detector. Warmer is the detector and smaller is the applied bias voltage in absolute value, smaller will be the t_p-value. Note that this effect is reversible in the sense that a short time depolarization of the detectors is enough to suppress the spectral degradation effects.

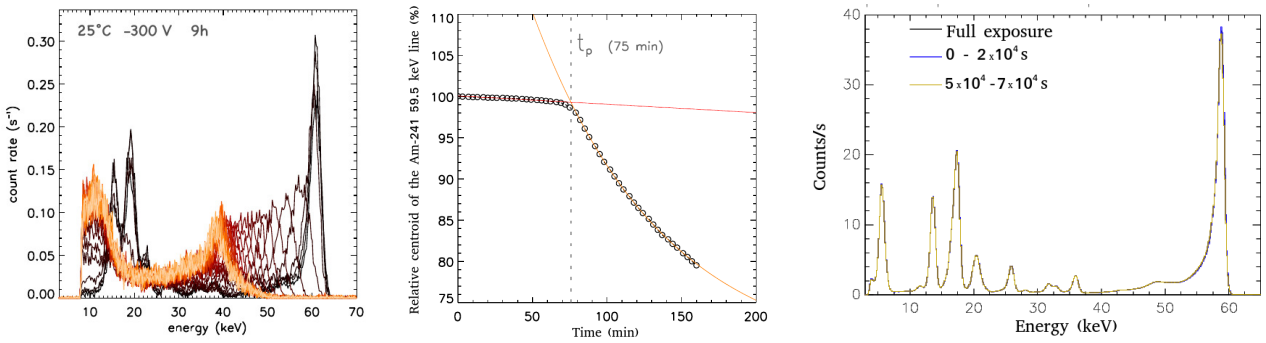

Figure 18. Left – Illustration of the polarization effect on the spectral response for one module detector. Data collected by illuminating an XRDPIX module with a ^{241}Am source during 9 h [27]. The detectors were biased at –300 V and operated at +25°C. The spectrum in light orange is the final one. Middle – Evolution of the relative value of the ^{241}Am 59.5 keV line centroid over 9 h [27]. t_p is the polarization time i.e. the time when the electric field cancels at the cathode. Right – Evolution of the single event ^{55}Fe + ^{241}Am spectra for ELS1 over 20 h. Data collected on the ECLAIRs detection plane. The detectors were cooled down at –15°C and biased at –300 V. There is no evidence for any spectral degradation induced by the polarization effect.

As mentioned in Section 1.2, the ECLAIRs detectors will be depolarized each time the satellite will go through a deep SAA passage. The maximum time interval without depolarizing the detectors is $\sim$ 15 h. In order to investigate whether the polarization may be an issue or not in flight, we performed a 20 h measure on the detection plane alone illuminated with ^{55}Fe + ^{241}Am radioactive sources. The detectors were cooled down to –15°C, a temperature higher than the nominal detector temperature range of ECLAIRs (see Section 1.2) and biased at –300 V. The right panel in Figure 18 shows the evolution of the spectral response for ELS1 over time. No significant degradation of the spectral response is observed. Similar results are obtained for the other sectors of the detection plane.

The performance stability vs detector temperature – We also took benefit of this measure to investigate the stability of the spectral response of each sector when changing the detector temperature. The left panel in Figure 19 compares the single event energy-calibrated spectra for ELS4 acquired on the detection plane illuminated with ^{55}Fe + ^{241}Am radioactive sources and a detector temperature of $T_{det} = -15°C$ (black) & $T_{det} = -20°C$ (red). There is a very good stability of the spectral response with the detector temperature for all sectors.

During the TVAC tests on the complete instrument (including the full thermal control system), we also performed measures illuminating the camera with ^{55}Fe + ^{241}Am sources for different detector thermal control

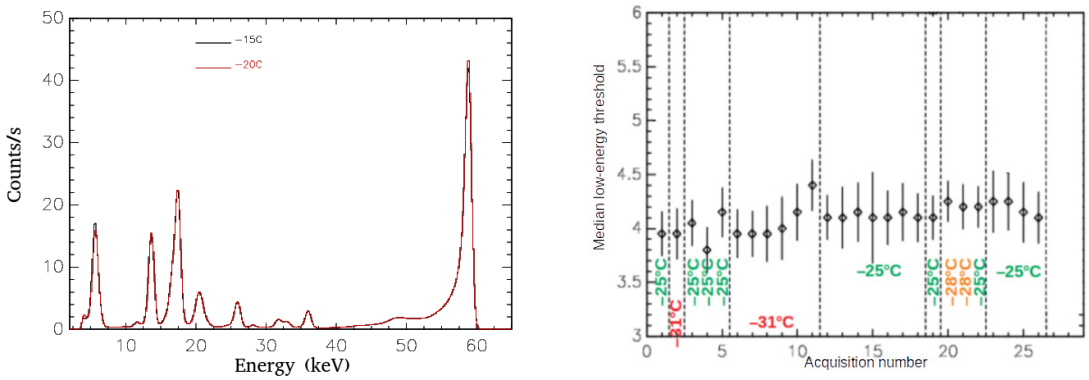

Figure 19. Left – Comparison of two single event energy-calibrated ^{55}Fe + ^{241}Am spectra for ELS4 acquired at two detector temperatures: $T_{det} = -15°C$ (black) & $T_{det} = -20°C$ (red). Right – Median low-energy threshold measured from the single event energy-calibrated spectra per XRDPIX module on the detection plane during the TVAC tests at different target temperatures T_{target}. The vertical bars on each datapoint correspond to the dispersion on the measured low-energy threshold distribution. Here the temperature values correspond to the target temperatures to reach by the regulating thermal system.

configurations. For each measure, we built the single event energy-calibrated spectra per module i.e. (200 spectra). We used spectra per module instead of per pixel to save some computation time as well as because of the very good homogeneity of the spectral response of the detectors (see Section 4.3). For each spectrum we then derived the value of the low-energy threshold (E_{th}) and we finally built E_{th}-histograms from which we computed the median and dispersion values. The right panel in Figure 19 shows the resulting evolution of the median E_{th}-values for each TVAC measure. The vertical bars on each datapoint indicates the dispersion. Note the overall good stability of the low-energy threshold in keV with temperature and over time. These results are compliant with our science requirements.

The stability over time – We also performed a week-long observing sequence with the ECLAIRs camera operated as it will do in space in order to test for the performance & system stability. ECLAIRs was operated under flight conditions including thermal variations (±3°C) along the orbit around a nominal temperature (see Figure 20A), variations of the incoming photon rates as well as realistic SAA passages (in term of duration, time spacing and number per day). During the deep SAA passages, the detectors were depolarized. At each exit, the dynamically disabled very noisy pixels were back to work. The camera was illuminated by both the X-ray fluorescence generator using various fluorescence targets (Cu, Ag, Mn, Ti, V & Sc) and ^{57}Co radioactive sources placed slightly off-axis within a sealed container in the thermal-vacuum chamber. This allowed to cover the full energy range of ECLAIRs. In order not to make any confusion between the 6.4 keV photons from the ^{57}Co sources and the low-energy fluorescence photons emitted by the X-ray generator, we added a kapton + Al layer in front of the Be window of the ^{57}Co container that absorbed more than 95% of the 6.4 keV photons. The X-ray fluorescence generator was used to modulate the incoming photon rate to simulate bursts & SAA entries (see Figure 20B). This allowed us to validate both the robustness and the resilience of the ECLAIRs system and onboard software. Figure 20C shows the single event energy-calibrated spectra for ELS1 acquired at different times when the incoming photon rates was stable. The only noticeable variation in the spectra is below 6 keV because of the SLE noise excess. The epochs when the SLE noise excess varied most were when the detector temperature was varying (see Figure 20B). Otherwise, note the very good stability of the spectral response over time. Similar results were obtained on the other sectors.

4.8 Imaging

As mentioned in Table 1, we were not able to measure the imaging performances of the camera due to constraints with our experimental setup, in particular to produce an X-ray source mimicking a point-like source at infinity. However, during the integration phases of the instrument, some alignment biases of the mask with respect to the plane have been measured. We also performed some measures with off-axis radioactive sources illuminating

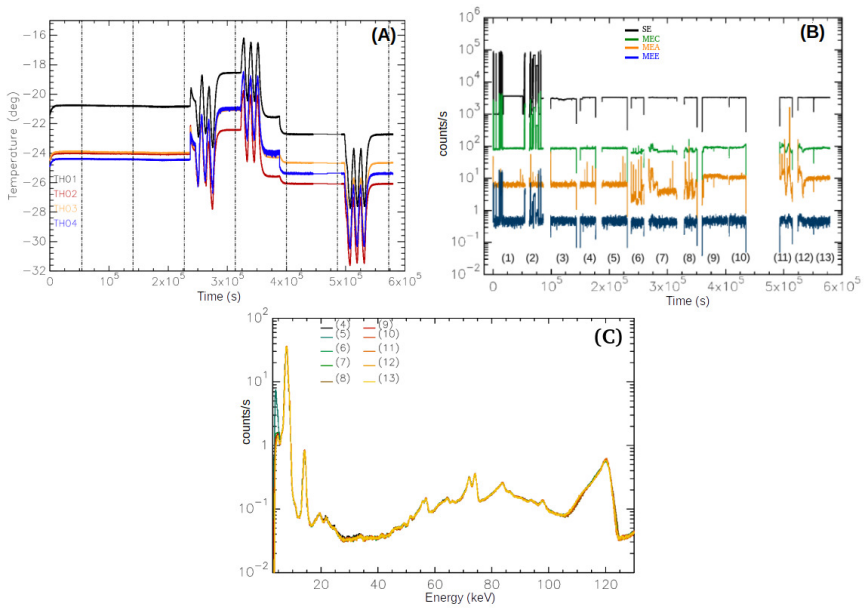

Figure 20. (A) Temperature profiles vs time. Temperature measures were collected at different locations on the cold plate around the detection plane. (B) Evolution of the count rates on the plane for different event types. The drops in count rate indicate the times when the detectors have been depolarized. (C) Superimposed single event energy calibrated spectra for ELS1 acquired at different times during the test.

the camera in order to make sure that the onboard software retrieved the right orientation of the reconstructed image; which was the case. Figure 21 shows a shadowgram acquired with an almost on-axis radioactive source (left), the pattern of the coded mask highlighting the part that has been projected onto the plane (middle) and the reconstructed image (right) showing the source right at the center as expected – see [26] for more details. The full characterization of the ECLAIRs imaging capabilities will be done during the commissioning phase using astrophysical targets.

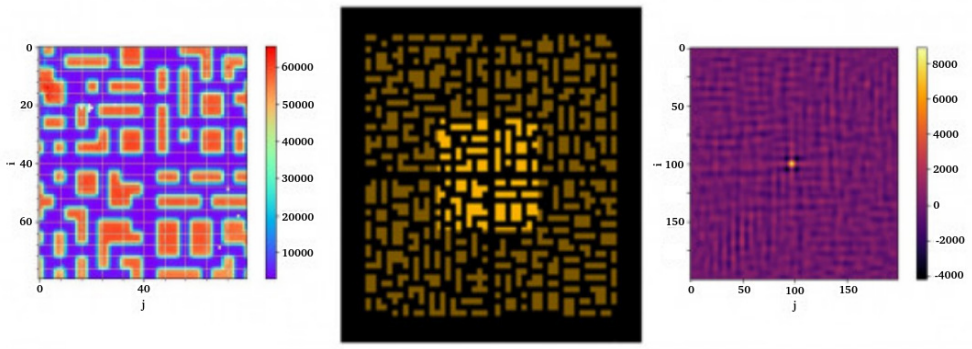

Figure 21. Left – Single event shadowgram for an almost on-axis radioactive source. Middle – Pattern of the coded mask with the area projected onto the plane highlighted. Right – Image reconstructed by the onboard software.

5. CONCLUDING REMARKS

We presented an overview of the performances measured during the different test sequences performed on the fight model of the ECLAIRs camera throughout 2021. Thanks to a careful upstream preparation of the test sequences and calibration activities on the flight model between the AIT and science teams, all the test sequences

went smoothly and nicely. We gathered all the data needed to calibrate the numerical models of ECLAIRs built using GEANT4-based simulations.

We demonstrated that most detectors on the plane have electronic noise allowing to reach a 4 keV energy threshold and this for the first time for a pixalated GRB trigger camera! This achievement was made possible by successfully hybridizing at IRAP the Acrorad Schottky-type CdTe detectors with the CEA-Saclay IDeF-X ASIC. Moreover, the Schottky-type CdTe detectors display very good and homogeneous performances. We showed that the overall performances of the camera are very stable over time and are compliant with our science requirements (see Figure 3). We also demonstrated our ability to accurately set the camera configuration, in particular the low-energy threshold.

There is presently on-going work to build the onboard configuration files that will be loaded in the UGTS prior to the launch and the calibration files that will be used for data reduction and analysis.

With a launch at the end of 2023, we actively prepare the calibration activities to be performed during the commissioning phase that will help us refining the above files.

REFERENCES

[1] Wei, J. et al., "The deep and transient universe in the SVOM era: New challenges and opportunities – scientific prospects of the SVOM mission," *arXiv:1610:06892* (2016).

[2] Zhang, B., "Gamma-ray bursts in the Swift era," *Chinese Journal of Astronomy and Astrophysics* **7**, 1 (2007).

[3] Godet, O. and Mochkovitch, R., "Afterglows after Swift," *Compte Rendu Physique* **12**, 276 (2011).

[4] Cucchiara, A. et al., "A photometric redshift of z $\sim$ 9.4 for GRB 090429b," *ApJ* **736**, 12 (2011).

[5] MacFadyen, A. I. and Woosley, S. E., "Collapsars: Gamma-ray bursts and explosions in failed supernovae," *ApJ* **524**, 262 (1999).

[6] Eichler, D. et al., "Nucleosynthesis, neutrino bursts and gamma-rays from coalescing neutron stars," *Nature* **340**, 126 (1989).

[7] Abbott, B. P. et al., "Gravitational waves and gamma-rays from a binary neutron star merger: GW 170817 and GRB 170817a," *ApJL* **848**, L13 (2017).

[8] Gehrels, N. et al., "The Swift Gamma-Ray Burst Mission," *ApJ* **611**, 1005 (2004).

[9] Godet, O. et al., "The X-/gamma-ray camera eclairs for the gamma-ray burst mission svom," in [*Space Telescopes and Instrumentation 2014: Ultraviolet to Gamma Ray*], *Proc. of SPIE* **9144**, 914424 (2014).

[10] Dong, Y. et al., "SVOM gamma ray monitor," *Science China Physics, Mechanics and Astronomy* **53**, 40 (2010).

[11] Wen, X. et al., "Calibration study of the Gamma-Ray Monitor onboard the SVOM satellite," *NIM-A* **1003**, 165301 (2021).

[12] Gotz, D. et al., "The microchannel x-ray telescope status," in [*Space Telescopes and Instrumentation 2016: Ultraviolet to Gamma Ray*], *Proc. of SPIE* **9905**, 99054L (2016).

[13] Meuris, A. et al., "The camera of the Microchannel X-ray Telescope onboard the svom mission," in [*Space Telescopes and Instrumentation 2014: Ultraviolet to Gamma Ray*], *Proc. of SPIE* **9144**, 91444Z (2014).

[14] Fan, X. et al., "The Visible Telescope onboard the Chinese-French SVOM satellite," in [*Space Telescopes and Instrumentation 2020: Optical, Infrared, and Millimeter Wave*], *Proc. SPIE* **11443**, 114430Q (2020).

[15] Han, X. et al., "The automatic observation management system of the GWAC network. i. System architecture and workflow," *PASP* **133**, 065001 (2021).

[16] Basa, S. et al., "COLIBRI, a wide-field 1.3 m robotic telescope dedicated to the transient sky," *Proc. of SPIE* (2022).

[17] NouveldelaFlèche, A. et al., "Flux reconstruction for the NIR camera CAGIRE at the focus of the telescope colibri," *Proc. of SPIE* (2022).

[18] Godet, O. et al., "Monte-carlos imulations of the background of the coded-mask camera for X- and gamma-rays on-board the Chinese-French GRB mission SVOM," *NIM-A* **603**, 365 (2009).

[19] Lacombe, K. et al., "Development of a 32-detector cdte matrix for the SVOM ECLAIRs X/gamma camera: Preliminary results," *Nuclear Instruments and Methods in Physics Research A* **732**, 122 (2013).

[20] Gevin, O. et al., "IDeF-X ECLAIRs: A CMOS ASIC for the readout of CdTe and CdZnTe detectors for high resolution spectroscopy," *IEEE Transactions on Nuclear Science* **56**, 2351 (2009).

[21] Gevin, O. et al., "IDeF-X v1.0: A new 16-channel low-noise analog front-end for Cd(Zn)Te detectors," *Nuclear Instruments and Methods in Physics Research A* **567**, 140 (2006).

[22] Gevin, O. et al., "IDeF-X ECLAIRs: An ultra low noise CMOS ASIC for the readout of Cd(Zn)Te detectors," in [*Nuclear Science Symposium Conference Record*], NSS, ed., *Proc. of IEEE* **1**, 326 (2007).

[23] Dagonneau, N. et al., "Onboard catalogue of known x-ray sources for SVOM/ECLAIRs," *A&A* **645**, 18 (2021).

[24] Bajat, A. et al., "Calibration of the spectral response of the SVOM/ECLAIRs detection plane," in [*Space Telescopes and Instrumentation 2018: Ultraviolet to Gamma Ray*], *Proc. of SPIE* **10699**, 106995J (2018).

[25] Bajat, A. et al., "Characterizing the dead time of the eclairs camera on board the mission svom," *Experimental Astronomy* **46**, 337 (2018).

[26] Schanne, S. et al. *in preparation* .

[27] Nasser, G., "Performence characterization of XRDPIX modules on the SVOM/ECLAIRs camera." http://thesesups.ups-tlse.fr/2945/1/2015TOU30221.pdf. Thesis defended in 29 September 2015.

[28] Lacombe, K. et al., "Spectral performance of ECLAIRs flight detectors on SVOM mission," *Astroparticle Physics* **103**, 131 (2018).

[29] Bajat, A., "Study of the dead-time and spectral response of the SVOM/ECLAIRs camera." http://thesesups.ups-tlse.fr/4060/1/2018TOU30151.pdf. Thesis defended in 9 October 2018.

[30] Bouchet, L. et al. *in preparation* .

[31] Cola, A. and Farella, I., "The polarization mechanism in CdTe Schottky detectors," *Applied Physics Letters* **94**, 102113 (2009).